

Intrinsic Conductance of Domain Walls in BiFeO₃

Yi Zhang, Haidong Lu, Xingxu Yan, Xiaoxing Cheng, Lin Xie, Toshihiro Aoki, Linze Li, Colin Heikes, Shu Ping Lau, Darrell G. Schlom, Longqing Chen, Alexei Gruverman,* and Xiaoqing Pan*

Ferroelectric domain walls exhibit a number of new functionalities that are not present in their host material. One of these functional characteristics is electrical conductivity that may lead to future device applications. Although progress has been made, the intrinsic conductivity of BiFeO₃ domain walls is still elusive. Here, the intrinsic conductivity of 71° and 109° domain walls is reported by probing the local conductance over a cross section of the BiFeO₃/TbScO₃ (001) heterostructure. Through a combination of conductive atomic force microscopy, high-resolution electron energy loss spectroscopy, and phase-field simulations, it is found that the 71° domain wall has an inherently charged nature, while the 109° domain wall is close to neutral. Hence, the intrinsic conductivity of the 71° domain walls is an order of magnitude larger than that of the 109° domain walls associated with bound-charge-induced bandgap lowering. Furthermore, the interaction of adjacent 71° domain walls and domain wall curvature leads to a variation of the charge distribution inside the walls, and causes a discontinuity of potential in the [110]_p direction, which results in an alternative conductivity of the neighboring 71° domain walls, and a low conductivity of the 71° domain walls when measurement is taken from the film top surface.

Ferroelectric domain walls are 2D structural boundaries that separate regions with different orientations of electrical polarization domains,^[1] which exhibit functional characteristics that are completely different from the domains that they delineate. For example, it has been shown that they may be metallic^[2] or even superconducting,^[3] while the domains that they separate

are insulating. Recent research shows that the domain walls can exhibit their own distinct chemistry and magnetic behavior.^[4–9] These emergent characteristics have fostered the realization that the domain walls can be used as functional elements in novel nanoelectronic devices.^[10–13] Here, we report observation of the intrinsic conductance of the 71° and 109° domain walls by probing the local conductance over a cross section of the BiFeO₃/TbScO₃ (001) thin-film heterostructures. Through a combination of conductive atomic force microscopy (CAFM), high-resolution electron energy loss spectroscopy (EELS), and phase-field simulations, we show that the 71° domain walls exhibit conductivity, which is about an order of magnitude larger than that of the 109° domain walls. More importantly, we demonstrate high anisotropy of the 71° domain walls' conductance; while they are conducting along the [010]_p direction, they show much lower conductance along the [001]_p direc-

tion. High-resolution EELS reveals a bandgap lowering at the 71° domain walls and only a little change at the 109° domain walls. The phase-field simulations reveal a charged nature of the 71° walls compared to almost neutral 109° walls, suggesting that charge-induced bandgap lowering is the main mechanism behind the intrinsic conductance of the 71° domain walls.

Dr. Y. Zhang, Dr. X. X. Yan, Dr. L. Xie, Dr. L. Z. Li, Prof. X. Q. Pan
Department of Materials Science and Engineering
University of California Irvine
Irvine, CA 92697, USA
E-mail: xiaoqinp@uci.edu

Dr. H. D. Lu, Prof. A. Gruverman
Department of Physics and Astronomy & Nebraska Center
for Materials and Nanoscience
University of Nebraska
Lincoln, NE 68588, USA
E-mail: agruverman2@unl.edu

Dr. X. X. Cheng, Prof. L. Q. Chen
Department of Materials Science and Engineering
Pennsylvania State University
State College, PA 16802, USA

Dr. T. Aoki
Irvine Materials Research Institute
University of California
Irvine, CA 92697, USA

Dr. C. Heikes, Prof. D. G. Schlom
Department of Materials Science and Engineering
Cornell University
Ithaca, NY 14850, USA

Prof. S. P. Lau
Department of Applied Physics
The Hong Kong Polytechnic University
Hung Hom, Kowloon 999077, Hong Kong

Prof. D. G. Schlom
Kavli Institute at Cornell for Nanoscale Science
Ithaca, NY 14853, USA

Prof. X. Q. Pan
Department of Physics and Astronomy
University of California
Irvine, CA 92697, USA

 The ORCID identification number(s) for the author(s) of this article can be found under <https://doi.org/10.1002/adma.201902099>.

DOI: 10.1002/adma.201902099

Furthermore, it is found that the conductance of the 71° walls alternates between the adjacent walls due to the electrostatic-interaction-induced potential distribution variation. The origin of the anisotropic conductance of the 71° walls stems from the potential discontinuity of the 71° domain walls along the $[110]_p$ direction. It is emphasized that the domain wall conductance measured in the direction normal to the film surface—experimental geometry used in most of the previous works—does not reveal the true conductance of the 71° domain walls.

A single-phase multiferroic BiFeO_3 (BFO) is the material where the intriguing electrical conductivity of the domain walls has been first reported.^[14–16] Since then, numerous studies have been performed to investigate the conducting properties of the 71° and 109° walls. The experimental results generally indicate that the 71° domain walls are more insulating as compared with the 109° walls.^[17–19] Lubk et al.^[20] suggested that the domain wall conductivity in BFO originated from the lowering of the bandgap at the walls, with the bandgap change at the 109° walls being larger than at the 71° walls. Several other mechanisms have been proposed, such as flexoelectric effect, octahedral rotation, oxygen vacancy migrating, chemical doping, domain wall geometry, and charge defect.^[21–26] However, two main issues remain to be addressed. First, most of the BFO materials in these studies are either defect-rich or element doped, which makes it difficult to separate the intrinsic conductivity of the domain walls from the effects of extrinsic factors.^[17,22,26,27] Second, in the previous studies, the domain wall conductivity is usually measured in the direction perpendicular to the film surface, i.e., by applying an electrical bias between the bottom electrode and the probing tip in contact with the domain wall.^[9,17] In this geometry, the results may be affected by domain wall discontinuity, inhomogeneous defect, and charge distributions at the domain walls, or domain wall bending and curving.^[28,29] Because of these factors, there was a strong variation in the transport properties of BFO domain walls reported in the previous works.^[17,21,27,30–33] Hence, for better understanding of the origin of the intrinsic domain wall conductivity, the deployment of experimental geometry and samples with carefully controlled electrical boundary conditions and domain structure is highly desirable.

In this work, the electrical transport properties of the as-grown 71° and 109° domain walls in the $\text{BiFeO}_3/\text{TbScO}_3$ (001) thin-film heterostructures have been studied by means of CAFM along two directions, i.e., parallel to and perpendicular to the film surface. We employ a multimodal testing approach based on a combination of piezoresponse force microscopy (PFM) and aberration-corrected transmission electron microscopy (TEM) characterization of the same specimens. This approach allows cross-correlation analysis of the TEM, PFM, and CAFM data enabling direct comparison of the domain wall conductance with the local polarization configuration, structural defects, and local chemistry at the atomic scale.

The 200 and 400 nm thick $(001)_p$ -oriented BFO thin films with ordered 71° and 109° domain structures grown by molecular-beam epitaxy (MBE) on insulating $(110)_o$ TbScO_3 (TSO) single-crystalline substrates have been used in this study (p and o subscripts represent pseudocubic and orthorhombic indices, respectively). Details of film growth are given in Experimental Section. The representative reflection high-energy electron diffraction (RHEED) pattern acquired during the film growth suggests a

high degree of film quality (Figure S1, Supporting Information). The regular PFM and cross-sectional high-resolution high-angle annular dark-field scanning transmission electron microscopy (HAADF-STEM) images demonstrate the high-ordered domain structures and the single crystalline with few defects in our BFO samples (Figures S2 and S3, Supporting Information).

The atomic-scale energy-dispersive X-ray spectroscopy (EDS) mapping further reveals that all types of domain walls have the similar chemical composition as the surrounding bulk sample without obvious defects or vacancies (Figures S2 and S3, Supporting Information). To test the domain wall conductance, we carried out PFM and CAFM mapping on the cross sections of the BFO/TSO heterostructures cut perpendicular to the 71° or 109° domain stripes (Figure 1a,f). Details of the specimen preparation and the schematic of the geometry of the CAFM measurements are discussed in ref. [34]. In Figure 1b, the vertical PFM image acquired on the sample cross section shows typical 71° periodical domain arrays, which is consistent with the bright-field TEM image (Figure S2, Supporting Information). We note that the domain width is not uniform in the ordered 71° domain arrays but changes periodically. Two adjacent and relatively close walls are labeled as DW1 and DW2, respectively (Figure 1b). Upon close examination, a slight curvature of the walls at the top interface vicinity can be seen. Figure 1c shows a CAFM image of the same region as in Figure 1b, which was acquired under an applied dc bias of 2 V. The CAFM contrast shows a strong current signal stemming from the 71° domain walls, indicating that these walls are conductive along the $[010]_p$ direction (which is parallel to the film surface). Interestingly, an alternating level of conductance can be observed at the adjacent 71° walls (Figure 1b,c), i.e., DW1 is more conductive than DW2. This difference is also clearly illustrated by the current profile line in Figure 1d. The I - V curves in Figure 1e further confirm this difference in conductance between the adjacent 71° domain walls.

Conductance of 109° walls along the $[010]_p$ direction was examined exactly in the same way (Figure 1f). The vertical PFM image of the 109° domain structure on the sample cross section (Figure 1g) is consistent with the TEM data shown in Figure S3 (Supporting Information). In contrast to the 71° domain walls, CAFM mapping of the 109° walls did not reveal any current above the noise level (Figure 1h). (Note that the conducting behavior of the BFO/TSO interface induced by the ferroelectric polarization of BFO has been discussed elsewhere^[34]). The low-conducting nature of the 109° walls along the $[010]_p$ direction is illustrated by the current profile and the I - V spectroscopic measurements (Figure 1i,j). In addition, a difference in conductance between the 71° and 109° walls along the $[010]_p$ direction has been further demonstrated by testing the mixed domain regions in another sample (Figure S4, Supporting Information). Detailed analysis shows that the conductance of the 71° domain walls is at least an order of magnitude larger than that of the 109° domain walls.

The bandgap of domain walls is considered as a critical parameter determining their intrinsic conductance.^[20] However, in the case of BFO, it has not been measured experimentally yet. To fully address the origin of the intrinsic conductance of domain walls, the bandgaps of the 71° and 109° domain walls were analyzed by using atomic-resolution EELS (see the Supporting Information for details). High-resolution low-loss EELS line-scans were taken across the adjacent 71° walls

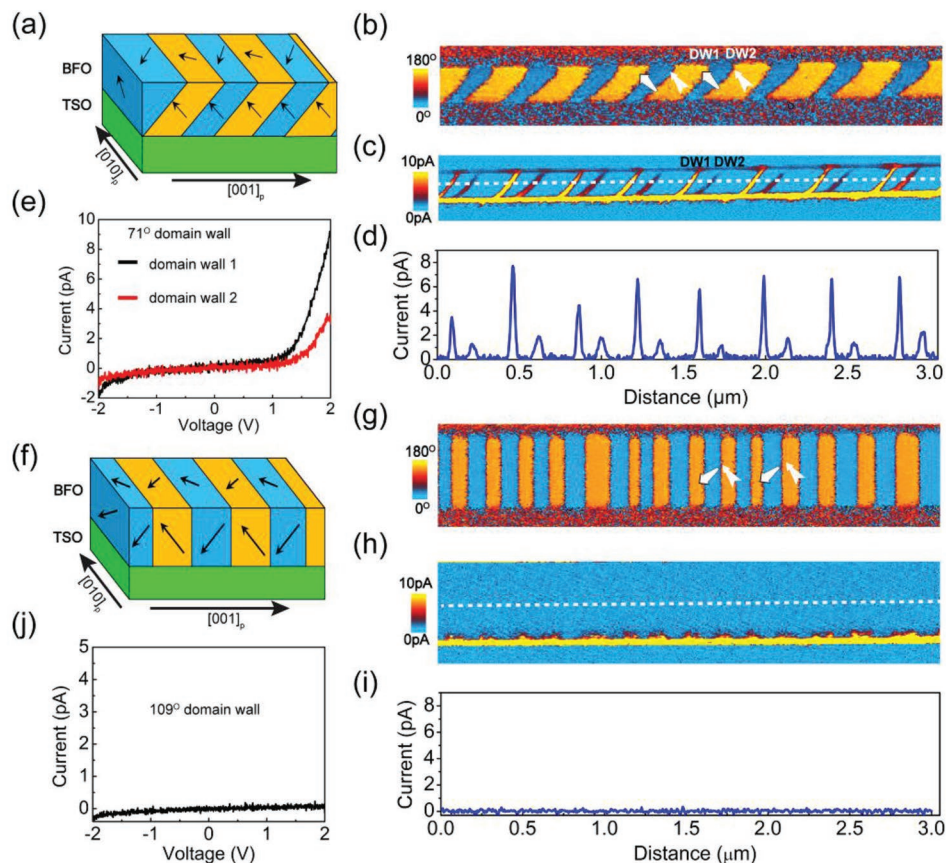


Figure 1. Conductance for the 71° and 109° domain walls on cross-sectional specimens. a) Schematic illustration of the 71° domain array. b) PFM phase image of cross-sectional BFO film with the 71° domain structure. The white arrows indicate the 3D polarization vector. c) CAFM image of the same region as in (b). d) The current profile along the white dotted line shown in (c). e) The I - V curves measured on 71° walls on the cross-sectional sample. f) Schematic illustration of 109° domain array. g) PFM phase image of cross-sectional BFO film with the 109° domain structure. h) CAFM image of the same region as in (g). i) The current profile along the white dotted line in (h). j) A typical I - V curve measured on the 109° wall on the cross-sectional sample. The sample thicknesses in $[010]_p$ direction in (a) and (f) are similar, which is around 1 μm .

(DW1 and DW2) and 109° domain wall (Figure 2a,d). The acquired results were averaged within the area along the domain walls. Bandgaps around two adjacent 71° domain walls and the 109° wall were calculated from the low-loss EELS results, as shown in Figure 2b,e. Details of the calculation of bandgap energy from the low-loss EELS can be found in Supporting Information. We can see an obvious bandgap lowering at the DW1 and DW2 compared to the bulk BFO, while little change is observed at the 109° domain walls. The lower bandgap of the 71° domain walls should lead to higher conductivity in agreement with our CAFM results. Consequently, the core-loss EELS was conducted across the walls and the energy onset difference between O- K and Fe- L_3 edges was extracted to elucidate the chemical shift of local Fe, since there is a linear relationship between this onset energy and the oxidation state of Fe.^[26,35] It is found that the energy onset difference of Fe-O at the 71° domain walls is lower than in bulk BFO, indicating a reduced valence state of Fe (Figure 2c). On the other hand, the energy onset difference of Fe-O at the 109° domain walls keeps intact with respect to the bulk phase (Figure 2f). Therefore, in contrast to the 109° walls, Fe at 71° domain walls (DW1 and DW2) has a reduced valence state donating electrons that

will compensate the possible bound charges at domain walls. We note that the bandgap reduction associated with charge accumulation has a visible difference between DW1 and DW2, which is consistent with the alternating conductance between the adjacent walls (Figures 1c and 2b,c).

It has been proposed that the oxygen vacancies play an important role in the conductivity of domain walls.^[29,36] To check if this mechanism is also applicable to our BFO films, EELS was used to examine oxygen vacancies at the BFO domain walls. EELS spectra in Figure S5 (Supporting Information) show no obvious evidence of oxygen vacancies around both 71° and 109° domain walls. Therefore, it can be concluded that oxygen vacancies are not the source of the domain wall conductivity observed in our experiments.

To further examine the domain walls' conductance, CAFM measurements have been carried out on the film top surface of the BFO/TSO heterostructure. As has been shown recently, a conductive BFO/TSO interface can be used as a bottom electrode.^[34] A typical pattern of the ordered 71° stripe domains has been revealed by lateral PFM (Figure 3a). We carried out CAFM mapping (Figure 3b) of the same region under an applied dc bias of ± 2 V and no current

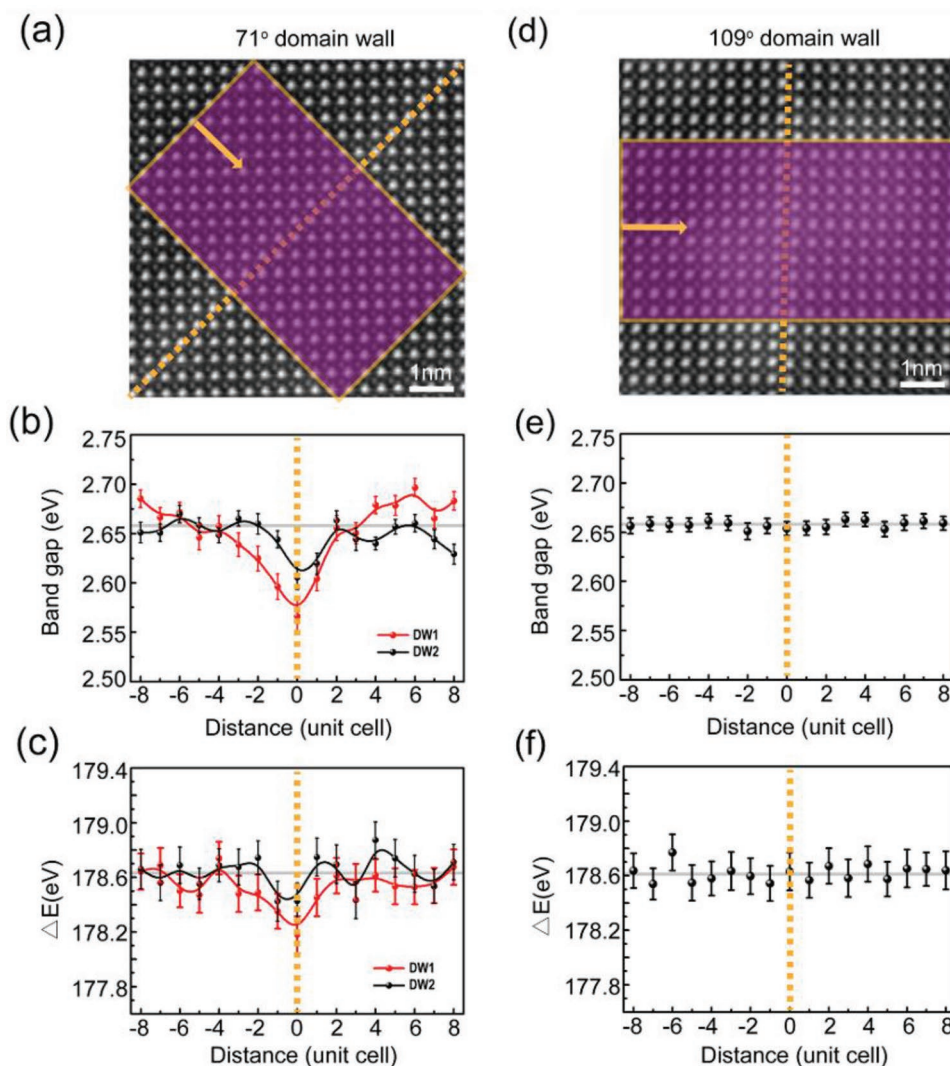


Figure 2. Bandgap and chemical profile at the adjacent 71° domain walls (DW1 and DW2) and 109° domain walls. a) HAADF-STEM image obtained at the region of 71° domain wall. The orange dashed line indicates the 71° domain wall. High-resolution EELS line scans were taken within the purple area in (a) and (d) along the directions indicated by the orange arrows, i.e., normal to the domain walls for both low-loss (b) and core-loss (c) measurements. b) A bandgap of two adjacent 71° domain walls (DW1 and DW2). The calculation of bandgap energy from low-loss EELS can be seen in the Methods. Figure S3 (Supporting Information) indexes the location of DW1 and DW2. c) The energy onset difference between O-K and Fe-L₃ edges (ΔE) across two adjacent 71° domain walls (DW1 and DW2). ΔE is related to Fe oxidation state. d) HAADF-STEM image obtained at 109° domain wall. The orange dashed line indicates the 109° domain wall. High-resolution EELS line scan was taken within the purple area along the scan direction of the orange arrow, which is vertical to the domain wall direction, for both low-loss (e) and core-loss (f) measurements. e) Bandgap of BFO across 109° domain wall. f) The energy onset difference between O-K and Fe-L₃ edges across the 109° domain wall. In (c)–(f), the vertical orange dashed lines indicate the location of corresponding domain walls. The gray dashed lines in (b) and (e) are located at 2.658 eV, which is average bandgap from BFO bulk. The gray dashed lines in (c) and (f) are located at 178.63 eV, which is average ΔE from BFO bulk.

signal could be detected at the 71° domain walls. A quantitatively different behavior was observed in the BFO/TSO samples with the 109° domains. Figure 3c shows the vertical PFM image of the BFO top surface, revealing a typical 109° striped domain structure. The CAFM image in Figure 3d shows strong current contrast due to the conducting 109° domain walls in agreement with the previously reported results.^[17,26,27] The conductivity difference between the 71° and 109° domain walls measured from the film top surface was further confirmed by *I*–*V* curves (see Figure S6 in the Supporting Information).

CAFM results from the cross-sectional samples confirm that 71° domain walls are generally more conducting than 109° domain walls. However, CAFM data collected in conventional geometry from the film top surface show that 109° domain walls are conducting, while 71° domain walls are insulating. Thus, it appears that both 71° and 109° domain walls show anisotropic conductance. However, in the case of 109° domain walls, the obtained results can be explained simply by the different thicknesses of the tested samples: conductivity is observed in the conventional geometry when the tip–electrode distance is 400 nm (Figure 3d) while no current was detected in

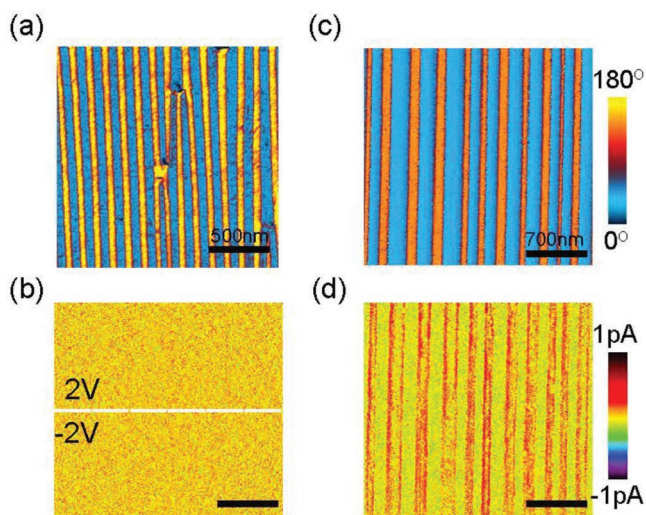


Figure 3. Conductance for the 71° and 109° domain walls measured from film surface in BFO/TSO structure. The thicknesses of the films with 71° and 109° domain are 200 and 400 nm, respectively. a) Lateral PFM phase image showing 71° domain structure. b) CAFM image of the same region as in (a). c) Vertical PFM phase image showing 109° domain structure. d) CAFM image of the same region as in (c).

the cross-sectional geometry when the tip–electrode distance was more than $1\ \mu\text{m}$ (Figure 1g). For the 71° walls, the situation is opposite; the conductivity measured on the cross-sectional surface (Figure 1c) is much larger than that detected on the film top surface (Figure 3b). Thus, it can be concluded that in the case of the 71° walls, we indeed observe genuine anisotropic conductance and not the thickness-induced effect. In addition, we test the BFO samples with 20 nm $\text{La}_{0.7}\text{Sr}_{0.3}\text{MnO}_3$ (LSMO) buffer layer at the interface in the same way, as shown in Figures S7 and S8 (Supporting Information). The conductance behaviors of the 71° and 109° domain walls in the sample with LSMO buffer layer are similar to the sample without LSMO layer.

To clarify a mechanism of the unusual conducting behavior of the 71° walls, phase-field modeling of the charge distribution in the ordered 71° and 109° domain arrays has been carried out^[11] (see the Supporting Information for details). The simulated domain structures of the 71° and 109° domains are shown in Figure 4a,d. For the 71° domains' simulations, we initially assume that the domain walls are planar, and the width of the adjacent domains, a and b , is the same (Figure 4a). In the following, we mark the neighboring 71° domain walls as domain wall 1 (DW1) and domain wall 2 (DW2). For the uniform domain width of 150 nm, i.e., a/b is 150/150, the simulation results show that the bound charge accumulates both at the

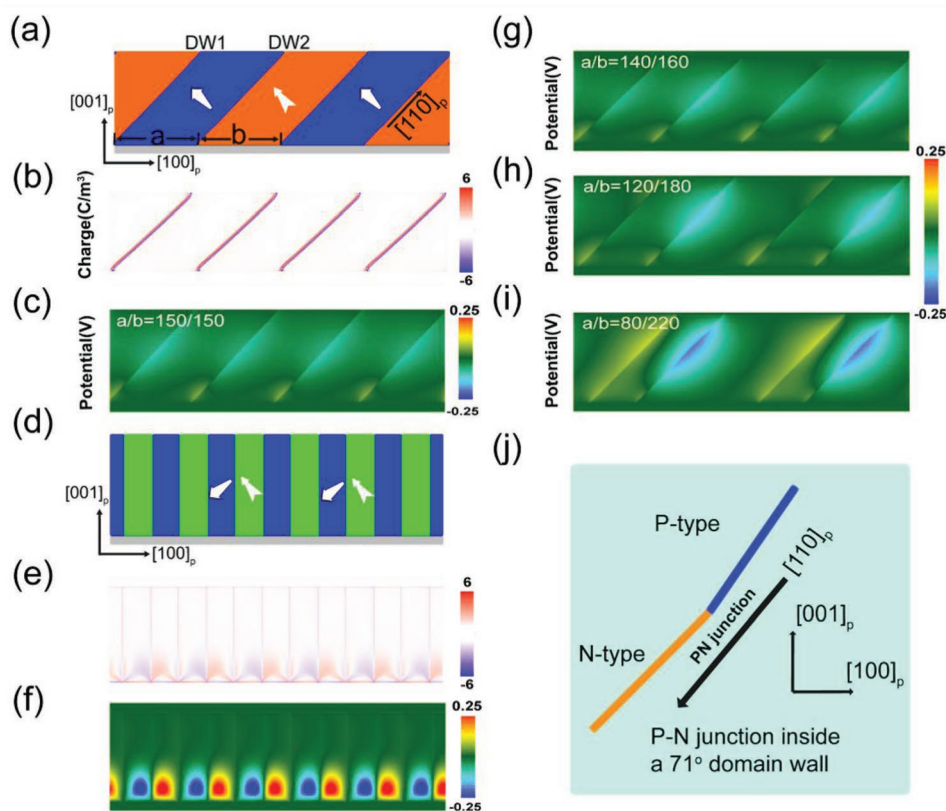


Figure 4. Phase-field simulations of the bound charge and potential distribution along the walls. a) The 71° domain arrays used for phase-field simulations. The widths of the two neighboring domains are expressed as a and b , respectively. The white arrows indicate the 3D polarization vector. b) The bound-charge distribution and c) the corresponding potential distribution around 71° domain walls separating domains of equal width. d) The 109° domain arrays used for phase-field simulations. e) The bound-charge distribution and f) the corresponding potential distribution around 109° domain walls. g–i) Potential distribution around 71° domain walls separating domains of different width with a/b ratios of 140/160 (g), 120/180 (h), and 80/220 (i). j) Schematic illustration of the p–n junction formed within a single 71° domain wall due to the wall bending.

DW1 and DW2, clearly distinguishing them from the interior of the domain region (Figure 4b). In contrast, in the 109° domain structure (Figure 4d), the charge distributes across the domain interior with few accumulations at the domain walls (Figure 4e). Therefore, even in the absence of any structural defects, a typical 71° domain wall is inherently charged, while a 109° domain wall is more close to being neutral. The difference in the bound charge distribution between the 71° and 109° domain walls is further illustrated by the line profiles across the walls (Figure S9, Supporting Information). The corresponding potential distributions at the 71° and 109° domain walls induced by the bound charge are shown in Figures 4c and 4f, respectively. It can be seen that the 71° walls exhibit a high potential, while the potential is close to zero at the 109° walls. Just like a charged domain wall, the 71° domain wall contains a higher density of bound charges than the 109° wall, which naturally should be compensated by more free carriers.^[36] The remarkable difference in bound charge accumulation and electric potential distribution between the 71° and 109° domain walls explains their drastically different intrinsic conductance. It should be also noted that the potential distribution is discontinuous along the 71° domain walls (i.e., $[110]_p$ direction) in the direction from the film/substrate interface to the film surface.

To clarify the origin of the conductance difference between the adjacent 71° domain walls, the previous phase-field model was expanded by considering the effect of uneven width of the adjacent domains (Figure 4a). When the a/b ratio gradually changes from 150/150 to 100/200, i.e., the domain becoming narrower, the potential of the DW1 turns more positive, while that of DW2 becomes partially negative (Figure 4g–i). The potential profiles along the domain walls in the $[110]_p$ direction changing with the a/b ratio are shown in Figure S10 (Supporting Information). Naturally, the strong positive potential leads to electron accumulation and results in high conductance of the DW1. In contrast, a low positive potential attracts fewer electrons and leads to lower conductivity in the DW2. Therefore, we believe that the difference conductance of the adjacent 71° domain walls stems from the electrostatic interaction between the adjacent walls across the narrower domain. The difference in conductance between the adjacent 71° domain walls agrees with the EELS and CAFM results in Figures 2 and 1, respectively.

In our experiments, the averaged a/b ratio was estimated to be in the range between 130/170 and 110/190. For this kind of domain configuration, we note that the potential distribution is generally not continuous along the $[110]_p$ direction according to the simulation results. As schematically shown in Figure 4j, this discontinuity of potential distribution may induce a potential barrier along the wall forming a p–n junction, which will obstruct the conducting path along the 71° domain walls in the film thickness direction (i.e., $[110]_p$ direction) when measurement is taken on the film top surface. Moreover, the domain wall curving induced by the domain wall tilting can also induce a local potential change and strengthen the potential discontinuity along the 71° domain walls in $[110]_p$ direction^[29] (see Figure S11 in the Supporting Information). We can see that the tilting of only the DW2 will cause the increasing of positive potential in both adjacent walls. In this case, the larger tilting angle will lead to larger conductance. In our sample, the 71° domain wall tilt mainly occurs at the bottom segment of DW2,

so that the domain wall curving induced by the local tilting strengthen the potential discontinuity along the $[110]_p$ direction. Therefore, the local tilting of domain wall could serve as another source of the alternating and anisotropic conductance of the 71° domain walls.

Thus, according to the phase-field simulation results, the conducting channel along the 71° domain walls in the film thickness direction is likely perturbed by the potential discontinuity, which explains the absence of the CAFM signal in Figure 3b. Therefore, their anisotropic conductance does not contradict the general conductive nature of the 71° domain walls. The potential discontinuity induced by the 71° domain wall curvature may be another reason behind the controversy regarding the conflicting reports on the conductance of the 71° domain walls.^[17–19,28,29]

In conclusion, using a combination of the local probe techniques, we have revealed the intrinsic conductivity of the 71° and 109° domain walls in BFO thin films, mainly derived from polarization-induced charge accumulation on the walls. We have found that the intrinsic conductivity of the 71° domain walls is an order of magnitude larger than that of the 109° domain walls. Atomic resolution EELS analysis and phase-field simulation demonstrate a clear bandgap lowering and a weakly charged nature of the 71° domain walls, while a little bandgap change is observed at the 109° walls. Furthermore, the electrostatic interaction^[37] of the neighboring 71° domain walls and the domain wall curvature can induce an inhomogeneous potential distribution along the $[110]_p$ direction, which induces strongly anisotropic conductance of the 71° walls: the insulating or poor conducting behavior along the $[110]_p$ direction and high conductivity in the $[010]_p$ direction. These results deepen our knowledge on the intrinsic conductivity of the BFO domain walls and may help explain the previous discrepancies regarding the reported variations in domain wall conductivity as well as the role of domain walls in the photovoltaic effect.^[16,17,19,38] Due to their anisotropic conductivity, the 71° and 109° domain walls can be used as a new type of local reconfigurable doping elements in the BFO matrix.^[27,39,40] This finding, while providing new insights into the fundamental physics of ferroelectric domain walls, may open a possibility for realization of domain wall-based devices with substantially enhanced functionality.

Experimental Section

Materials' Synthesis and Characterization: The BiFeO₃ films were grown on single-crystalline (110)_o TbScO₃ substrates by reactive MBE. The 200 and 400 nm thick BiFeO₃ film were deposited at 650 °C in distilled ozone (≈80% ozone) at $pp = 4 \times 10^{-6}$ Torr. Cross-sectional TEM samples were prepared by conventional mechanical polishing followed by argon ion milling. The specimen's preparation for CAFM was the same with that of regular TEM. The thickness of the specimens for CAFM was of several micrometers; see the details in the Supporting Information. High spatial resolution STEM-EELS experiments were performed by Nion UltraSTEM 200 at UC, Irvine, equipped with C3/C5 corrector, and high-energy resolution monochromated EELS system (HERMES). The instrument was operated at 100 kV with convergence semiangle of 30 mrad and with a beam current of ≈100 pA. Atomic-resolution EDS mapping was performed on JEOL JEM-ARM300CF S/STEM, equipped with double correctors and dual high-speed high-solid angle silicon drift detectors (SDDs), under a convergence semiangle of 22 mrad.

Supporting Information

Supporting Information is available from the Wiley Online Library or from the author.

Acknowledgements

Y.Z., H.D.L., and X.X.Y. contributed equally to this work. The work was supported by the U.S. Department of Energy, Office of Basic Energy Sciences, Division of Materials Sciences and Engineering under Grant DE-SC0014430 (Y.Z., X.X.Y., L.Z.L., L.X., and X.Q.P.). The research at the University of Nebraska-Lincoln was supported by the National Science Foundation through the Nebraska Materials Science and Engineering Center (MRSEC, Grant No. DMR-1420645) and by Grant No. DMR-1709237 (H.D.L. and A.G.). The work at Penn State was supported by the U.S. Department of Energy, Office of Basic Energy Sciences, Division of Materials Sciences and Engineering under Award DE-FG02-07ER46417. The work at Cornell University was supported by the National Science Foundation (Nanosystems Engineering Research Center for Translational Applications of Nanoscale Multiferroic Systems) under Grant Number EEC-1160504 (C.A.H. and D.G.S.). Substrate preparation was performed in part at the Cornell Nanoscale Facility, a member of the National Nanotechnology Coordinated Infrastructure (NNCI), which was supported by the National Science Foundation (Grant No. ECCS-1542081). The work in Hong Kong was supported by the Hong Kong Polytechnic University grants (I-ZVGH). The authors would like to acknowledge the use of the advanced TEM facilities in the Irvine Materials Research Institute (IMRI) at the University of California, Irvine.

Conflict of Interest

The authors declare no conflict of interest.

Keywords

conductive atomic force microscopy, domain walls, ferroelectric films, intrinsic conductance, piezoresponse force microscopy

Received: April 2, 2019

Revised: June 30, 2019

Published online: July 28, 2019

- [1] J. M. Gregg, A. Kumar, *Nature* **2014**, *510*, 481.
- [2] T. Sluka, A. K. Tagantsev, P. Bednyakov, N. Setter, *Nat. Commun.* **2013**, *4*, 1808.
- [3] A. Aird, E. K. H. Salje, *J. Phys.: Condens. Matter* **1998**, *10*, 377.
- [4] S. Farokhipoor, C. Magén, S. Venkatesan, J. Íñiguez, C. J. M. Daumont, D. Rubi, E. Snoeck, M. Mostovoy, C. de Graaf, A. Müller, M. Döblinger, C. Scheu, B. Noheda, *Nature* **2014**, *515*, 379.
- [5] J. Seidel, G. S. Bhalla, Q. He, S. Y. Yang, Y. H. Chu, R. Ramesh, *Phase Transitions* **2013**, *86*, 53.
- [6] M. P. Campbell, J. P. V. McConville, R. G. P. McQuaid, D. Prabhakaran, A. Kumar, J. M. Gregg, *Nat. Commun.* **2016**, *7*, 13764.
- [7] Z. Gareeva, O. Dieguez, J. Iniguez, A. K. Zvezdin, *Phys. Rev. B* **2015**, *91*, 060404.
- [8] T. Sluka, A. K. Tagantsev, P. Bednyakov, N. Setter, *Nat. Commun.* **2013**, *4*, 1808.
- [9] J. Guyonnet, I. Gaponenko, S. Gariglio, P. Paruch, *Adv. Mater.* **2011**, *23*, 5377.
- [10] G. Catalan, J. Seidel, R. Ramesh, J. F. Scott, *Rev. Mod. Phys.* **2012**, *84*, 119.
- [11] L. Z. Li, J. Britson, J. R. Jokisaari, Y. Zhang, C. Adamo, A. Melville, D. G. Schlom, L. Q. Chen, X. Q. Pan, *Adv. Mater.* **2016**, *28*, 6574.
- [12] C. C. Ju, J. C. Yang, C. Luo, P. Shafer, H. J. Liu, Y. L. Huang, H. H. Kuo, F. Xue, C. W. Luo, Q. He, P. Yu, E. Arenholz, L. Q. Chen, J. Zhu, X. Lu, Y. H. Chu, *Adv. Mater.* **2016**, *28*, 876.
- [13] J. Seidel, M. Trassin, Y. Zhang, P. Maksymovych, T. Uhlig, P. Milde, D. Köhler, A. P. Baddorf, S. V. Kalinin, L. M. Eng, X. Q. Pan, R. Ramesh, *Adv. Mater.* **2014**, *26*, 4376.
- [14] J. C. Yang, Q. He, P. Yu, Y. H. Chu, *Annu. Rev. Mater. Res.* **2015**, *45*, 249.
- [15] J. Seidel, R. K. Vasudevan, N. Valanoor, *Adv. Electron. Mater.* **2016**, *2*, 1500292.
- [16] S. Y. Yang, J. Seidel, S. J. Byrnes, P. Shafer, C. H. Yang, M. D. Rosse, P. Yu, Y.-H. Chu, J. F. Scott, J. W. Ager, L. W. Martin, R. Ramesh, *Nat. Nanotechnol.* **2010**, *5*, 143.
- [17] J. Seidel, L. W. Martin, Q. He, Q. Zhan, Y.-H. Chu, A. Rother, M. E. Hawkrigde, P. Maksymovych, P. Yu, M. Gajek, N. Balke, S. V. Kalinin, S. Gemming, F. Wang, G. Catalan, J. F. Scott, N. A. Spaldin, *Nat. Mater.* **2009**, *8*, 229.
- [18] H. W. Jang, D. Ortiz, S. H. Baek, C. M. Folkman, R. R. Das, P. Shafer, Y. B. Chen, C. T. Nelson, X. Q. Pan, R. Ramesh, C. B. Eom, *Adv. Mater.* **2009**, *21*, 817.
- [19] Y. P. Chiu, Y. T. Chen, B. C. Huang, M. C. Shih, J. C. Yang, Q. He, C. W. Liang, J. Seidel, Y. C. Chen, R. Ramesh, Y. H. Chu, *Adv. Mater.* **2011**, *23*, 1530.
- [20] A. Lubk, S. Gemming, N. A. Spaldin, *Phys. Rev. B* **2009**, *80*, 104110.
- [21] S. Farokhipoor, B. Noheda, *Phys. Rev. Lett.* **2011**, *107*, 127601.
- [22] P. Maksymovych, J. Seidel, Y. H. Chu, P. Wu, A. P. Baddorf, L. Q. Chen, S. V. Kalinin, R. Ramesh, *Nano Lett.* **2011**, *11*, 1906.
- [23] G. Catalan, *Ferroelectrics* **2012**, *433*, 65.
- [24] J. Seidel, P. Maksymovych, Y. Batra, A. Katan, S.-Y. Yang, Q. He, A. P. Baddorf, S. V. Kalinin, C. H. Yang, J. C. Yang, Y. H. Chu, E. K. H. Salje, H. Wormeester, M. Salmeron, R. Ramesh, *Phys. Rev. Lett.* **2010**, *105*, 197603.
- [25] R. K. Vasudevan, A. N. Morozovska, E. A. Eliseev, J. Britson, J.-C. Yang, Y.-H. Chu, P. Maksymovych, L. Q. Chen, V. Nagarajan, S. V. Kalinin, *Nano Lett.* **2012**, *12*, 5524.
- [26] T. Rojac, A. Bencan, G. Drazic, N. Sakamoto, H. Ursic, B. Jancar, G. Tavcar, M. Makarovic, J. Walker, B. Malic, D. Damjanovic, *Nat. Mater.* **2016**, *10*, 4799.
- [27] A. Crassous, T. Sluka, A. K. Tagantsev, N. Setter, *Nat. Nanotechnol.* **2015**, *10*, 614.
- [28] N. Choudhury, L. Walizer, S. Lisenkov, L. Bellaiche, *Nature* **2011**, *470*, 513.
- [29] A. Tselev, P. Yu, Y. Cao, L. R. Dedon, L. W. Martin, S. V. Kalinin, P. Maksymovych, *Nat. Commun.* **2016**, *7*, 11630.
- [30] S. Prosandeev, Y. Yang, C. Paillard, L. Bellaiche, *npj Comput. Mater.* **2018**, *4*, 8.
- [31] R. K. Vasudevan, Y. Cao, N. Laanait, A. Ilevlev, L. Li, J. C. Yang, Y. H. Chu, L. Q. Chen, S. V. Kalinin, P. Maksymovych, *Nat. Commun.* **2017**, *8*, 1318.
- [32] P. Sharma, Q. Zhang, D. Sando, C. H. Lei, Y. Liu, J. Li, V. Nagarajan, J. Seidel, *Sci. Adv.* **2017**, *3*, e1700512.
- [33] J. Jiang, Z. L. Bai, Z. H. Chen, L. He, D. W. Zhang, Q. H. Zhang, J. A. Shi, M. H. Park, J. F. Scott, C. S. Hwang, A. Q. Jiang, *Nat. Mater.* **2018**, *17*, 49.
- [34] Y. Zhang, H. Lu, L. Xie, X. Yan, T. R. Paudel, J. Kim, X. Cheng, H. Wang, C. Heikes, L. Li, M. Xu, D. G. Schlom, L. Chen, R. Wu, E. Y. Tsybal, A. Gruverman, X. Q. Pan, *Nat. Nanotechnol.* **2018**, *13*, 1132.
- [35] H. Y. Tan, J. Verbeeck, A. Abakumov, G. V. Tendeloo, *Ultramicroscopy* **2012**, *24*, 116.
- [36] T. Sluka, A. K. Tagantsev, D. Damjanovic, M. Gureev, N. Setter, *Nat. Commun.* **2012**, *3*, 748.
- [37] A. V. Ilevlev, S. Jesse, A. N. Morozovska, E. Strelcov, E. A. Eliseev, Y. V. Pershin, A. Kumar, V. Y. Shur, S. V. Kalinin, *Nat. Phys.* **2014**, *10*, 59.
- [38] H. Matsuo, Y. Kitanaka, R. Inoue, Y. Noguchi, M. Miyayama, T. Kiguchi, T. J. Konno, *Phys. Rev. B* **2016**, *94*, 214111.
- [39] E. A. Eliseev, A. N. Morozovska, G. S. Svechnikov, P. Maksymovych, S. V. Kalinin, *Phys. Rev. B* **2012**, *85*, 045312.
- [40] P. Maksymovych, *Nat. Nanotechnol.* **2015**, *10*, 571.